Case Studies in Construction Materials 22 (2025) e04198

Contents lists available at ScienceDirect

Case Studies in Construction Materials

journal homepage: www.elsevier.com/locate/cscm

Sustainable Asphalt Mixtures Reinforced with Basic Oxygen Furnace Steel Slag: Multi-Scale Analysis of Enhanced Interfacial Bonding

Bin Lei [a,b], Linjie Yu [a], Jiawu Chen [a], Yuan Meng [c], Dong Lu [c,*], Ning Li [d], Fulin Qu [b,*]

[a] School of Infrastructure Engineering, Nanchang University, Nanchang 330031, China
[b] Centre for Infrastructure Engineering and Safety, School of Civil and Environmental Engineering, The University of New South Wales, NSW 2052, Australia
[c] Department of Civil and Environmental Engineering, The Hong Kong Polytechnic University, Hung Hom, Kowloon, Hong Kong
[d] Department of Solids and Structures, University of Manchester, Manchester M13 9PL, United Kingdom

ARTICLE INFO

Keywords:
Basic oxygen furnace steel slag
Asphalt mixtures
Interface transition zone
Fractal dimension
Multi-scale analysis
Sustainable pavement

ABSTRACT

Utilizing Basic Oxygen Furnace Slag (BOFS) to enhance the pavement performance of the asphalt mixtures is a promising strengthening strategy. However, the academic literature still needs to explore the interfacial dynamics and underlying mechanisms. This study introduces fractal dimension analysis to quantify the Interfacial Transition Zone (ITZ) characteristics in asphalt mixtures incorporating BOFS. A multi-scale analysis of the ITZ performance was conducted on three types of asphalt mixtures: Full Proportion Steel Slag Asphalt Mixture (100SSA-AM), Full Proportion Basalt Asphalt Mixture (100NCA-AM), and Asphalt Mixture of Coarse Aggregate Steel Slag and Fine Aggregate Basalt (Hybrid-AM). The results indicate that compared to the conventional 100NCA-AM, the splitting tensile strength and cracking index of 100SSA-AM and Hybrid-AM increased by 22.2 %, 28.1 %, and 13.5 %, 7.1 %, respectively. The total porosity of 100SSA-AM and Hybrid-AM increased by 58.4 % and 47.2 %, respectively, while the fractal dimension of the pores slightly decreased. In addition, compared to 100NCA-AM and 100SSA-AM, the ITZ fractal dimension of Hybrid-AM increased by 7.03 % and 3.79 %, respectively. In terms of interfacial nanomechanics, the ITZ indentation modulus of 100SSA-AM increased by 14.6 %, and the ITZ width increased by 43.5 % compared to 100NCA-AM, whereas for Hybrid-AM, the ITZ indentation modulus increased by 43.5 % and the ITZ width decreased by 26.1 %. Moreover, the study further revealed that the width and nanomechanical properties of the ITZ are closely associated with the surface roughness and chemical affinity of the aggregates, which holds significant implications for the design and application of sustainable pavement materials.

1. Introduction

The rapid growth of global infrastructure has led to an increasing demand for construction materials, resulting in a significant rise in the use of asphalt mixtures as the primary material for pavement construction [1–3]. However, the depletion of natural aggregate resources and the environmental challenges posed by the accumulation of industrial by-products have driven the search for sustainable

---

* Corresponding authors.
E-mail addresses: dong71.lu@connect.polyu.hk (D. Lu), fulin.qu@unsw.edu.au (F. Qu).

https://doi.org/10.1016/j.cscm.2024.e04198
Received 24 October 2024; Received in revised form 18 December 2024; Accepted 31 December 2024

alternative materials [4–6]. Steel slag, a major by-product of the steelmaking process, presents a promising substitute for natural aggregates in asphalt mixtures due to its comparable physical and chemical properties [7,8].

Basic Oxygen Furnace Slag (BOFS) aggregate has a rough surface, complex texture, and large angularity, contributing to adequate internal friction within the aggregate-asphalt matrix system [9,10]. Additionally, the surface of BOFS contains a certain amount of micropores and a rich content of oxides such as FeO/Fe_2O_3[11,12]. Soroosh et al. indicated that BOFS-asphalt mixtures possess stronger water damage resistance than traditional ones [13]. Extensive research suggests that BOFS can enhance the mechanical properties and durability of asphalt mixtures while reducing the depletion of natural sand and stone resources [13–16]. Furthermore, other scholars have used materials such as glass powder [17], stamped sand, composite materials of acrylonitrile-styrene-acrylate plastic waste [18], waste rubber powder [19,20], and tyre fibres [21] to improve the performance of asphalt and its mixtures, achieving significant enhancement effects. However, applying these materials may involve more complex processing and recycling procedures. In comparison, using steel slag to enhance the asphalt-aggregate interface performance offers several distinct advantages, such as the low disposal cost of industrial waste steel slag and its high hardness and stiffness, which makes it particularly suitable for heavy traffic applications.

The Interface Transition Zone (ITZ) between aggregates and asphalt mortar is a critical area in asphalt mixtures [22]. Insufficient adhesion in the ITZ can directly lead to issues such as pavement cracking and water damage [23]. The presence of free calcium oxide and magnesium oxide on the surface of BOFS can trigger volume expansion reactions when exposed to water [24], which may negatively impact the adhesion between asphalt mortar and aggregates. Ameri et al. [25] observed that the crack resistance of BOFS-asphalt mixtures is slightly lower than that of conventional asphalt mixtures, attributing this difference to the distinct adhesion properties at the steel slag-asphalt interface compared to the limestone-asphalt interface.

Asphalt mixtures are classic examples of multiphase and anisotropic composite materials [26]. Investigating the interfacial behavior and interaction mechanisms of these mixtures through multi-scale analysis provides a deeper understanding of material behavior at the microscale, thereby optimizing macroscopic properties such as durability and crack resistance [27]. Jiang et al. [28] employed multi-scale analysis methods and imaging techniques, including Scanning Electron Microscopy (SEM), to study the filling characteristics of aggregates, enabling both visual and quantitative analysis of the internal structure of asphalt mixtures. Similarly, Wang et al. [29] analyzed the interfacial morphology and mechanical properties of conventional cold patch asphalt mixtures using multi-scale testing methods, offering a theoretical foundation for repairing potholes in asphalt pavements.

Current research primarily focuses on either micro-scale material damage or macro-scale pavement deterioration in BOFS-asphalt mixtures, with limited attention to multi-scale analysis of ITZ performance. The interaction mechanisms at the BOFS and asphalt-mortar interface, particularly from a multi-scale perspective, remain inadequately understood. The chemical composition, physicochemical properties, and morphological characteristics of aggregates are key factors influencing interfacial adhesion [30]. A multi-scale analysis of the differences in interfacial bonding and mechanical properties arising from the substitution of natural aggregates with BOFS can provide deeper insights into the mechanisms of damage, deformation, and performance degradation in steel slag pavement materials.

This study utilizes multi-scale analysis methods to thoroughly investigate the intrinsic mechanisms underlying the interface structure and performance evolution in BOFS-asphalt mixtures across three levels: aggregate, ITZ, and asphalt mixture. Initially, the macroscopic mechanical Indirect Splitting Test (IDT) is employed to analyze the fracture failure modes of asphalt mixtures containing BOFS and basalt, quantitatively assessing the bonding performance between the aggregate and asphalt-mortar interface. Subsequently, a systematic investigation of the pore size distribution and porosity in asphalt mixtures is conducted using X-ray Computed Tomography (X-CT) and Mercury Intrusion Porosimetry (MIP). The research then introduces the box-counting method from fractal geometry to quantify the fractal dimension of the ITZ contour. It further explores performance parameters such as chemical element distribution, interface roughness, and indentation modulus through Atomic Force Microscopy (AFM) and Energy Dispersive Spectroscopy (EDS) line scanning. The chemical composition and surface morphology of BOFS and basalt are compared using SEM and laser scanning confocal microscopy. Finally, the nanomechanical properties of the ITZ are investigated using nanoindentation (NI). This research provides significant insights and novel perspectives on the degradation patterns of interfacial properties in BOFS-asphalt mixtures, offering a theoretical foundation for the sustainable design and construction of road pavements.

2. Experimental program

2.1. Raw materials

Styrene-Butadiene-Styrene (SBS) modified asphalt, sourced from Weilong Petrochemical Co., Ltd., Maoming City, Guangdong Province, was used as the base material in this study. The SBS-modified asphalt was further enhanced with a High-Ductility, Ultra-Thin

Table 1
Basic properties of SBS-modified asphalt and DTO-asphalt.

Properties	SBS-modified asphalt	DTO-modified asphalt	Test methods
Penetration (25 ℃,100 g, 5 s) (0.1 mm)	47.9	49.1	T 0604–2011
Ductility (5 cm/min, 5 °C) (cm)	39.3	57.2	T 0605–2011
Softening point /℃	85.5	92.3	T 0606–2011
Dynamic viscosity at 60 ℃/ (Pa·s)	43772	391627	T 0620–2011

Overlay (DTO) modifier obtained from Shengguang Tuo Regenerate Science and Technology Co., Ltd., Beijing, resulting in a DTO variant. Both the SBS-modified and high-elasticity DTO-modified asphalt were evaluated in accordance with the JTG E20–2011 [31] specification, with their fundamental properties presented in Table 1. Ordinary limestone powder was used as the filler material. BOFS, with a maximum nominal particle size of 9.5 mm, was sourced from Lingshou County, Shijiazhuang City, Hebei Province. The BOFS underwent natural weathering for over six months before application, meeting the aggregate usage criteria outlined in JTG E42–2024 [32]. Basalt was selected as the reference aggregate. The properties of the BOFS and basalt aggregates across different size ranges are provided in Table 2.

Fig. 1(a)-(b) illustrate significant differences in the microstructure between basalt and BOFS. Specifically, the micro surface of basalt is characterized by flaky protrusions and basin-like depressions, which are relatively smooth and exhibit a flaky distribution. In contrast, the microtexture of BOFS is complex, the surface is rough, and it contains an abundance of micropores, beneficial for the interface bonding between asphalt and aggregate [12]. Fig. 1(c) shows that BOFS first exhibits an endothermic peak near 100 °C, primarily attributed to the evaporation of free water in weathered steel slag, resulting in mass loss [33]. Notably, the natural weathering accumulation of BOFS can produce gypsum ($CaSO_4\cdot 2\ H_2O$), and the dehydration transition to hemihydrate ($CaSO_4\cdot 0.5\ H_2O$) may also occur when the temperature is below 115 °C. Continuous heating can cause hemihydrate to further harden into γ-$CaSO_4$ under water pressure. However, when the water molecule pressure is insufficient, gypsum will directly transform into γ-$CaSO_4$ [34]. BOFS shows endothermic peaks at 393 °C and 729 °C, mainly related to the thermal decomposition of $Ca(OH)_2$ and $CaCO_3$. The mass loss variation of BOFS throughout the entire Thermogravimetry (TG) experimental process does not exceed 3 %, demonstrating excellent thermal stability. Typically, the alkalinity value, the ratio of CaO content to SiO_2 contents [35], is higher, which is more conducive to the chemical adhesion between asphalt and aggregate. Fig. 1(d) indicates that the highest content in BOFS is CaO, reaching 38 %, with SiO_2 content less than 17 %, whereas in basalt, the highest content is SiO_2, up to 48 %, and the CaO content is less than 12 %. This suggests that the chemical adhesive action between BOFS and weakly acidic asphalt is superior to that of basalt.

2.2. *Asphalt mixture design*

The asphalt mixture was designed according to the JTG E20–2011 [31] specification, with a maximum nominal aggregate size of 9.50 mm, using the Marshall compaction method. The experimental design included three groups: a full-scale basalt asphalt mixture (100NCA-AM) as the control group, a full-scale BOFS asphalt mixture (100SSA-AM), and a coarse BOFS-fine basalt asphalt mixture (Hybrid-AM), where BOFS was used for the 2.36–9.5 mm size range and basalt for the 0–2.36 mm range. To maintain consistency in the gradation curves across the 100NCA-AM, 100SSA-AM, and Hybrid-AM mixtures, the basalt and BOFS aggregates were sorted by size. This process involved crushing, dust removal, and screening, resulting in eight specific size ranges: 0–0.075 mm, 0.075–0.15 mm, 0.15–0.30 mm, 0.30–0.60 mm, 0.60–1.18 mm, 1.18–2.36 mm, 2.36–4.75 mm, and 4.75–9.50 mm.

Given that the density of BOFS is 1.2 times that of basalt, directly using the mass ratio as the volume ratio would lead to discrepancies between the actual and target gradation curves. To ensure comparable volume parameters for 100NCA-AM, 100SSA-AM, and Hybrid-AM, adjustments were made to account for the mass ratio of BOFS to basalt, following a method similar to that used by Ferreira et al. [36]. By converting and analyzing the mass passing rate and volume passing rate of the asphalt mixture gradation curves, the volume passing rates for the three asphalt mixtures were determined, as illustrated in Fig. 2. The dosages of the DTO modifier and mineral powder were set at 0.6 % and 6 % of the asphalt mixture's mass, respectively. The target air void content for 100NCA-AM was designed at 4.5 ± 0.2 %, with the Optimal Asphalt-to-Aggregate Content (OAC) calculated and experimentally verified to be 5.8 %. To maintain consistency, the OAC for both 100SSA-AM and Hybrid-AM was also set at 5.8 %.

2.3. *Experimental methods*

2.3.1. *Indirect tensile test*

To assess the bond strength between aggregates and asphalt mortar, the Indirect Tensile Test (IDT) was performed on 100NCA-AM, 100SSA-AM, and Hybrid-AM in accordance with the JTG E20–2011 [31] specification. The loading was displacement-controlled at a rate of 50 mm/min, with the test temperature set at 28°C. Each group of specimens was tested in quadruplicate. The IDT testing equipment used for asphalt mixtures is depicted in Fig. 3. The formulas for calculating the splitting tensile strength, failure strain, and stiffness modulus of the asphalt mixture are provided in Eqs. (1) and (2):

Table 2
Basic physical properties of BOFS and basalt.

	BOFS			Basalt			Test methods
Size range (mm)	9.5–4.75	4.75–2.36	2.36–0	9.5–4.75	4.75–2.36	2.36–0	
Bulk S.G	3.211	3.197	2.997	2.747	2.741	2.687	T 0304
Apparent S.G	3.489	3.475	3.427	2.855	2.846	2.796	T 0304
Water absorption (%)	2.6	2.7	2.8	0.3	0.4	0.4	T 0304
Abrasion loss (Log Angeles) (%)	13.3		–	15.7			T 0317
Crushing value (%)	12.3			12.6			T 0316
Volume expansion (%)	1.2			Not detected			T 6523

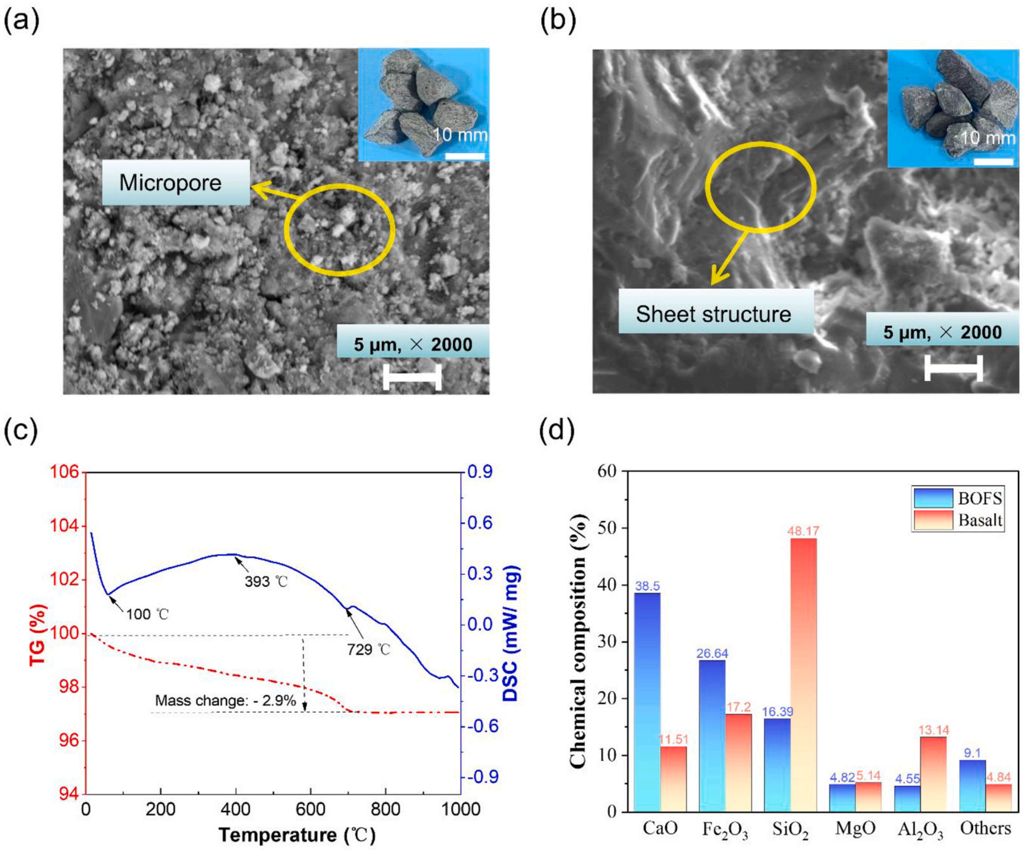

Fig. 1. Basic physicochemical properties of basalt and BOFS. (a) Microscopic appearances of BOFS. (b) Microscopic appearances of basalt. (c) TG analysis of BOFS. (d) Chemical composition.

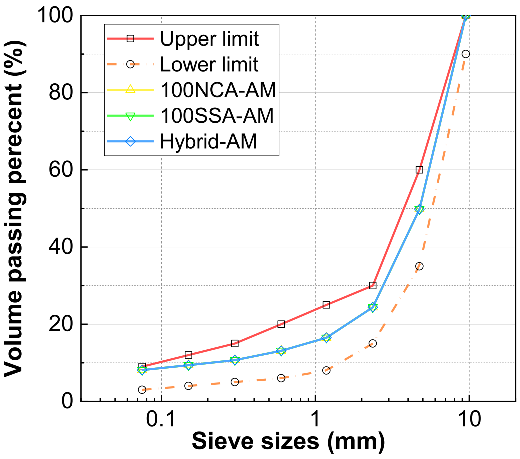

Fig. 2. The gradation curves of 100NCA-AM, 100SSA-AM and Hybrid-AM.

$$R_T = \frac{0.006287P_T}{h} \tag{1}$$

$$\varepsilon_T = X_T \times (0.0307 + 0.0936\mu)/(1.35 + 5\mu) \tag{2}$$

$$S_T = P_T \times (0.27 + 1.0\mu)/(h \times X_T) \tag{3}$$

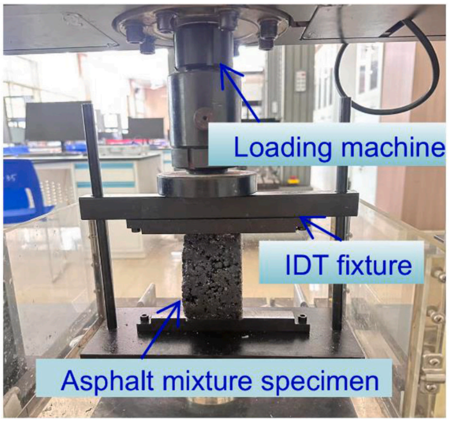

Fig. 3. IDT test equipment for asphalt mixture.

Where: R_T represents the splitting tensile strength, MPa; ε_T is the failure strain; S_T indicates the failure stiffness modulus, MPa; P_T denotes the maximum test load, N; X_T represents the total horizontal deformation at the failure load, mm; h is the specimen height, mm; μ is taken as 0.43.

To more accurately reflect the crack resistance of asphalt mixtures under actual service loads, Zhou et al. [37] proposed the concept of the cracking test index (CT_{index}) based on the typical load-displacement curve. The formula for calculating the cracking test index is given by Eq. (4).

$$CT_{index} = \frac{t}{62} \times \frac{G_f}{|m_{75}|} \times \frac{l_{75}}{D} \tag{4}$$

Where: t represents the specimen thickness, mm; G_f indicates the fracture energy, J/m^2; m_{75} is the slope of the load-displacement curve at the 75 % peak load point, KN/mm; l_{75} suggests the displacement at the 75 % peak load point, mm; D is the specimen diameter, mm.

2.3.2. MIP test

Mercury intrusion porosimetry (MIP) was employed to quantitatively analyze the pore structure and porosity of the asphalt mixtures. The MIP testing was conducted using the AutoPore V 9600, a fully automatic mercury porosimeter manufactured by Micromeritics Instrument Corporation, USA, capable of detecting pore diameters ranging from 3 nm to 1100 μm.

2.3.3. X-CT test

Non-destructive inspection of the asphalt mixtures was performed using a micro-focus X-ray CT system (Inspex Xio SMX-225CT) manufactured by Shimadzu Corporation, Japan. This equipment enables the analysis of the internal pore distribution and pore size structure of the asphalt mixtures. The experimental setup utilized a tube voltage of 220 kV, with standard Marshall specimens, each measuring 101.6 mm in diameter and 63.5 ± 1.3 mm in height. The pore distribution within the asphalt mixtures was obtained through 3D reconstruction of CT scan data, followed by image segmentation, denoising, and filtering using Avizo software. The processing method for the CT scan experimental data is illustrated in Fig. 4.

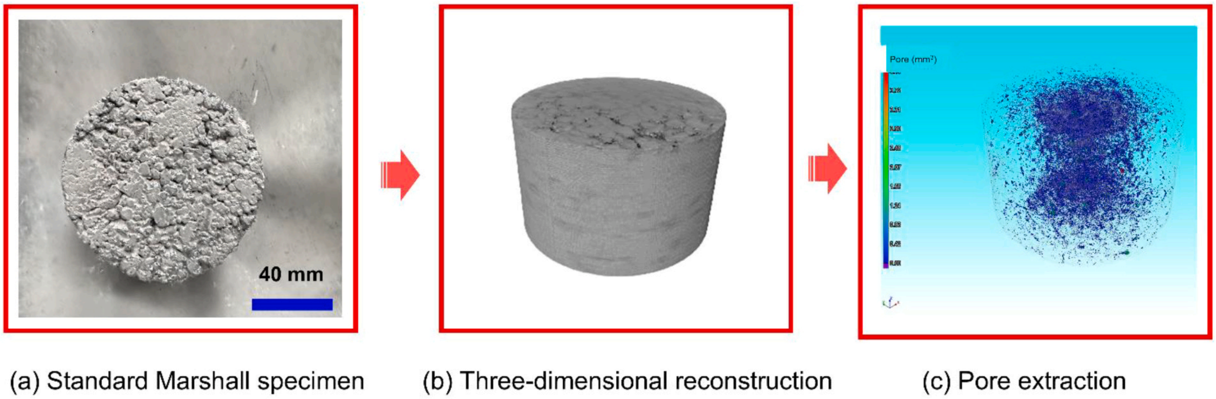

(a) Standard Marshall specimen (b) Three-dimensional reconstruction (c) Pore extraction

Fig. 4. Processing data steps of CT test for asphalt mixture.

2.3.4. *Laser scanning confocal microscopy*

To elucidate the influence of aggregate surface microstructure on the formation and degradation evolution of the ITZ, a laser scanning confocal microscopy (LSCM, ZEISS LSAM900) was utilized to analyze the surface morphology and microstructure of BOFS and basalt. BOFS and basalt surface characteristics, with particle sizes ranging from 2.36 to 9.5 mm, were examined through confocal scanning. The micro-surface morphology of the aggregates was characterized using the arithmetic mean height (S_a), root mean square roughness (S_q), and surface profile sharpness (S_{ku}). To mitigate the potential for experimental variability, each type of aggregate was tested in quadruplicate. S_a and S_q represent the extent to which the surface profile deviates from a reference line. S_{ku} is indicative of the height of the probability density distribution function of the surface profile at its mean value. Typically, a S_{ku} value below three denotes a relatively smooth surface. The formulas for calculating S_a, S_q, and S_{ku} are presented in Eqs. (5) to (7), respectively.

$$S_a = \frac{1}{n}\sum_{i=1}^{n}|y_i| \tag{5}$$

$$S_q = \sqrt{\frac{1}{n}\sum_{i=1}^{n}y_i^2} \tag{6}$$

$$S_{ku} = \frac{1}{nS_q^3}\sum_{i=1}^{n}y_i^3 \tag{7}$$

Where: y_i represents the contour deviation of the aggregate surface.

2.3.5. *Microscopy observation and elemental analysis test*

This study employed a scanning electron microscope (Carl Zeiss Gemini SEM 300) equipped with a high-performance EDS to collect micro-morphologies of the ITZ and adjacent areas randomly. Ten areas were sampled from each specimen, half at magnifications of 800x and 1000x. Image analysis software, Image J, was utilized to obtain the grayscale threshold lines of the images. After denoising and skeletonization, the interface contour lines between the aggregate and asphalt-mortar were acquired (as shown in Fig. 5(a)-(f)). The fractal dimension of the ITZ's contour in the asphalt mixture was analyzed by the box-counting method from fractal dimension theory. The box-counting method involves selecting a series of square boxes with decreasing side lengths S to cover the target set completely and counting the minimum number of boxes N that contain the set's characteristic values. The box dimension D can then be determined by fitting with image processing software, as illustrated in Fig. 5(g), with the calculation formula shown in Eq. (8) [38]:

$$D = -\frac{\log(N)}{\log(S)} \tag{8}$$

Where, D represents the box dimension, N is the minimum number of boxes required to cover the target area, and S denotes the scaling factor of the boxes.

EDS is a chemical characterization technique that relies on the interaction of X-ray excitation with materials and is often combined with SEM to analyze the elemental composition of asphalt concrete materials [39]. In this study, SEM-EDS was employed to examine

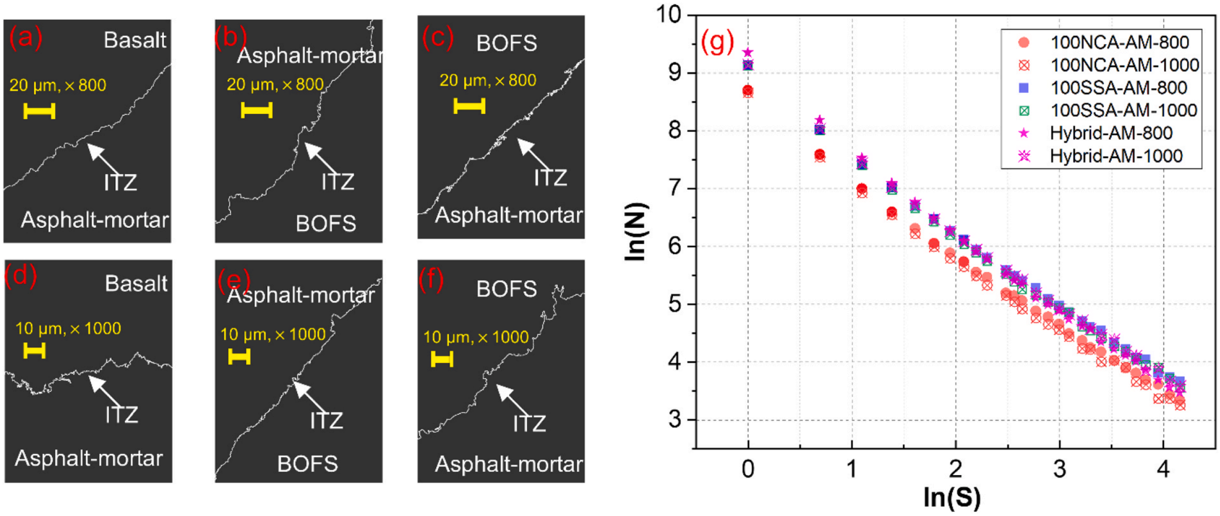

Fig. 5. SEM profile and voids count at the ITZ between aggregate and asphalt-mortar; (a) and (d) 100NCA-AM; (b) and (e) 100SSA-AM; (c) and (f) Hybrid-AM; (g) SEM profile and voids count.

the morphological characteristics, elemental composition, distribution, and width of the ITZ and its surrounding area. Specifically, SEM-EDS surface scanning was performed on the ITZ to map the distribution of eight elements (O, S, Fe, Al, Si, Ca, Mg, and C). Additionally, SEM-EDS line scanning was conducted on the same ITZ areas to generate variation curves of elemental signal intensities along the scanning line. The width of the ITZ was determined by analyzing the changes in elemental signals from the line scans, in conjunction with SEM micrographs and EDS surface scanning results.

2.3.6. AFM test

To gain a comprehensive understanding of the interfacial bonding between asphalt mortar and aggregate, as well as the three-dimensional interfacial morphology and roughness, Atomic Force Microscopy (AFM, Bruker Dimension Icon) from Bruker Corporation, Germany, was used to observe the microstructure of the ITZ. Standard small Marshall specimens were cut into rectangular samples measuring 15 × 15 × 8 mm using a numerically controlled laser stone-cutting machine. The sample surfaces were then made relatively flat through grinding and polishing. To prevent damage to the stylus, a gentle tapping mode was employed during the observation of the ITZ, with a scanning area set at 20 × 20 μm.

2.3.7. NI test

To evaluate the stiffness of the interfaces and the deformation resistance capabilities of asphalt mixture, nanoindentation tests were conducted on the ITZ produced by Hysitron, a US company. Fig. 6 illustrates the nanoindentation test scheme for the ITZ of the asphalt mixture. Strain-controlled testing was employed, with the maximum strain set to 200 nm, and the loading and unloading rate at adjacent test points was set to 10 nm/s, with a 2-second dwell at maximum displacement. Irregular nanoindentation curves were discarded, possibly due to large voids and cracks in the ITZ [40]. The elastic modulus (E) of the specimen is primarily determined from the force-displacement curve of the indenter penetration, and the material stiffness (S) is determined by the slope of the unloading force-displacement curve [41]. According to the power-law fitting method, the relationship between the material stiffness (S) and the reduced modulus (E_r) is obtained [42], as shown in Eq. (5). By substituting Eq. (9) into Eq. (10), the expression for the specimen's elastic modulus (E) is derived, as shown in Eq. (11).

$$S = \frac{dP}{dh} = \frac{2}{\sqrt{\pi}} E_r \sqrt{A_c} \tag{9}$$

$$\frac{1}{E_r} = \frac{(1 - r^2)}{E} + \frac{(1 - r_i^2)}{E_i} \tag{10}$$

(a) Standard Marshall specimens **(b)** Linear cutting machine **(c)** Coring specimen

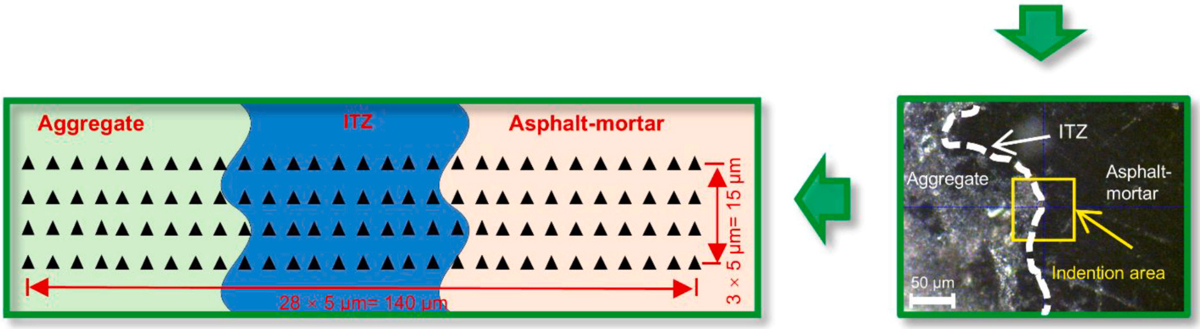

(e) Layout of testing points **(d)** Nanoindentation area

Fig. 6. Design of nanoindentation test for ITZ between aggregate and asphalt-mortar.

$$E = \left(1 - r^2\right) \times \left(\frac{2\sqrt{A_c}}{S \times \sqrt{\pi}} - \frac{1 - r_i^2}{E_i}\right)^{-1} \tag{11}$$

Where: A_c represents the maximum projected contact area between the indenter and the specimen in the axial direction at the peak load. γ denotes the Poisson's ratio of the specimen; E_i refers to the elastic modulus of the indenter; and γ_i signifies the Poisson's ratio of the indenter. For the experiments conducted, the indenter's elastic modulus (E_i) and Poisson's ratio (γ) are set at 1140 GPa and 0.30, respectively.

3. Results and discussion

3.1. *Macroscopic interface performance analysis*

3.1.1. *Tensile strength and failure strain*

Fig. 7 shows that the tensile strength of 100SSA-AM and Hybrid-AM increased by 22.2 % and 28.1 %, respectively, compared to 100NCA-AM, while their failure strain increased by 14.3 % and 5.9 %, respectively. This improvement can be attributed to several factors. First, the rough micro-surface structure of BOFS facilitates better mechanical interlocking with the asphalt, whereas the smoother surface of basalt reduces micro-level physical interlock points. Second, the high adhesiveness of BOFS to asphalt enhances the tensile strength of the asphalt-aggregate interface [43], while the relatively weaker bonding of basalt leads to reduced interfacial compatibility in the asphalt mixture. Notably, the high strength of coarse aggregates (BOFS) combined with the toughness and elasticity provided by fine aggregates (basalt) creates a complementary effect on the mechanical properties, allowing Hybrid-AM to exhibit superior flexibility under load.

3.1.2. *Stiffness modulus and cracking test index*

Fig. 8 illustrates the asphalt mixtures' crack resistance index and stiffness modulus. Typically, the crack resistance index ranges from 0 to 1000, with higher values indicating better crack resistance [37]. The results show that, compared to 100NCA-AM, the crack resistance index of 100SSA-AM and Hybrid-AM has increased by 13.5 % and 7.1 %, respectively. This is mainly due to the chemical properties of the basalt surface, which results in weaker compatibility with asphalt than BOFS, leading to a higher tendency for stress concentration in the ITZ. Additionally, the multi-angular and rough surface texture of BOFS enhances the crack resistance of the asphalt mixture by allowing better stress distribution under load, thereby suppressing crack initiation and propagation [44]. The stiffness modulus of 100SSA-AM is 31.3 % lower than that of Hybrid-AM, which may be attributed to the fine basalt aggregate filling the voids between BOFS. This improves the adhesion of asphalt to the aggregate surface, forming a stronger asphalt film and enhancing the structural strength and durability of the asphalt mixture.

3.2. *Microscopic pore structure characteristics*

3.2.1. *Pore structure characteristics*

Porosity and fractal dimension indicate the material's compactness and the complexity of its pore structure, respectively [45]. Tortuosity and permeability, on the other hand, reflect the complexity of the fluid flow path and the ease with which fluid passes through the pores; typically, higher tortuosity corresponds to lower permeability. The pore size structure characteristics of 100NCA-AM, 100SSA-AM, and Hybrid-AM are illustrated in Fig. 9(a)-(b).

Fig. 9(a) indicates that, compared to 100NCA-AM, the porosity of 100SSA-AM and Hybrid-AM increased by 58.4 % and 47.2 %,

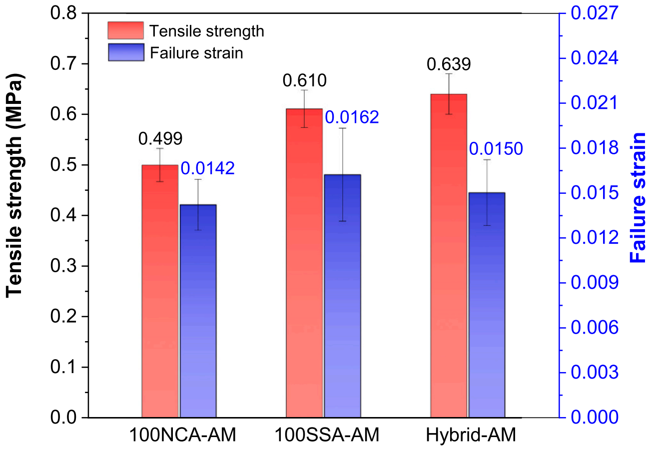

Fig. 7. Tensile strength and failure strain of 100NCA-AM, 100SSA-AM and Hybrid-AM.

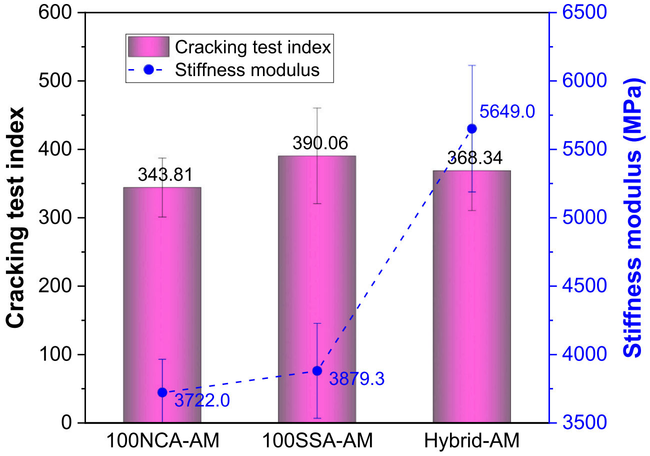

Fig. 8. Cracking test index and stiffness modulus of 100NCA-AM, 100SSA-AM and Hybrid-AM.

respectively, while the fractal dimension of pores decreased by 1.4 % and 1.1 %, respectively. This can be attributed primarily to the rough surface and irregular shape of BOFS, which result in a less compact internal structure in 100SSA-AM, leading to larger pores with a relatively simple distribution. In contrast, the smoother surface and regular shape of basalt promote a denser arrangement, reducing the porosity in 100NCA-AM but potentially leading to a more dispersed and complex pore structure. Additionally, the combination of the distinct aggregate characteristics of BOFS and basalt in Hybrid-AM results in porosity and fractal dimension values that fall between those of 100NCA-AM and 100SSA-AM.

Fig. 9(b) shows that, compared to 100NCA-AM, the tortuosity of 100SSA-AM and Hybrid-AM is reduced by 74.0 % and 27.5 %, respectively. However, the permeability of 100SSA-AM and Hybrid-AM is significantly higher than that of 100NCA-AM. This difference is mainly due to the distinct physical properties of BOFS and basalt, which influence the tortuosity and permeability of the asphalt mixtures. Specifically, BOFS exhibits higher porosity (5.5 percentage points higher than basalt [46]) and is characterized by straight-through large pores, which allows for relatively simple pore channels and favorable connectivity within 100SSA-AM. The dense and fine pore structure of basalt leads to tortuous and complex pore channels within 100NCA-AM, resulting in lower permeability. Interestingly, Hybrid-AM benefits from the large pores provided by coarse BOFS and the fine basalt that can fill the gaps between pores, making it easier to form complex pore channels.

3.2.2. *Distribution characteristics of pore area and pore volume*

Based on pore size, the pores are classified into visible pores and cracks (100–1000 μm), macropores (1–100 μm), mesopores (0.1–1 μm), small pores (0.01–0.1 μm), and micropores (0.001–0.01 μm) [47]. Fig. 10 illustrates the distribution characteristics of pore size, pore volume, and pore area within the asphalt mixture.

Fig. 10(a) indicates that as pore size increases, the cumulative mercury intrusion curves for 100NCA-AM, 100SSA-AM, and Hybrid-

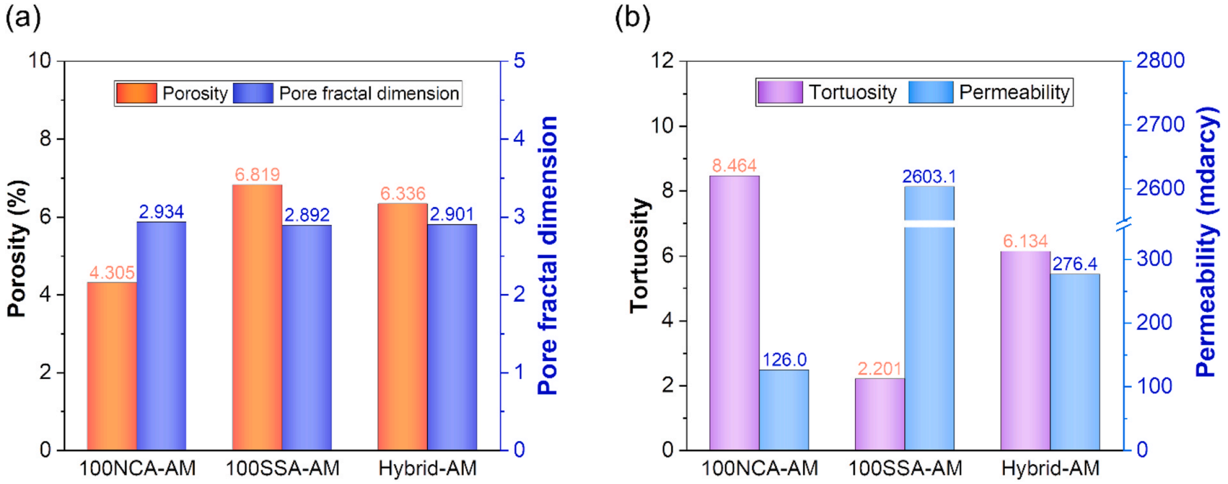

Fig. 9. Pore structure characteristics of 100NCA-AM, 100SSA-AM and Hybrid-AM: (a) Porosity and pore fractal dimension and (b) Tortuosity and permeability.

AM become progressively steeper. This is because, at low initial pressures, only larger pores, such as visible pores and macropores, are invaded and filled by mercury, while micropores and finer pores require higher pressures for mercury intrusion. Fig. 10(b) reveals that the internal pore distribution of 100NCA-AM, 100SSA-AM, and Hybrid-AM is predominantly composed of macropores and visible pores with diameters greater than 10 μm. This is largely due to the insufficient packing of aggregates, such as BOFS and basalt, and the incomplete filling by asphalt. The surface roughness and internal pore structure of BOFS and basalt significantly influence the arrangement of aggregates and the extent of asphalt filling [48]. Studies have shown that the volume proportion of BOFS pores larger than 1 μm exceeds 80 % [47], while for basalt, it exceeds 58 % [46].

Fig. 10(c) demonstrates that the volume proportion of micropores, small pores, and mesopores is significantly higher in Hybrid-AM compared to 100NCA-AM and 100SSA-AM. This increase is due to the rapid cooling required for BOFS, which must be cooled from a high temperature of 1600°C, necessary for the chemical reaction between coke and iron ore [49]. This rapid cooling results in more irregular fine pores within the internal structure. Additionally, basalt, with its naturally formed volcanic rock characteristics, typically features more prominent and uniform pores. Interestingly, as shown in Fig. 10(d), the proportion of micropore area in 100SSA-AM and Hybrid-AM is reduced by 7–15 percentage points compared to 100NCA-AM. This reduction is primarily because BOFS exhibits better adhesion to asphalt than basalt [50], and the viscosity and fluidity of asphalt partially fill the fine pores.

3.2.3. *Three-dimensional distribution of pore*

Standard Marshall specimens were subjected to X-CT scanning, followed by image preprocessing. Over 1150 CT scan slices from this experiment were converted into grayscale images. Porosity and pore characteristics were determined layer by layer by segmenting

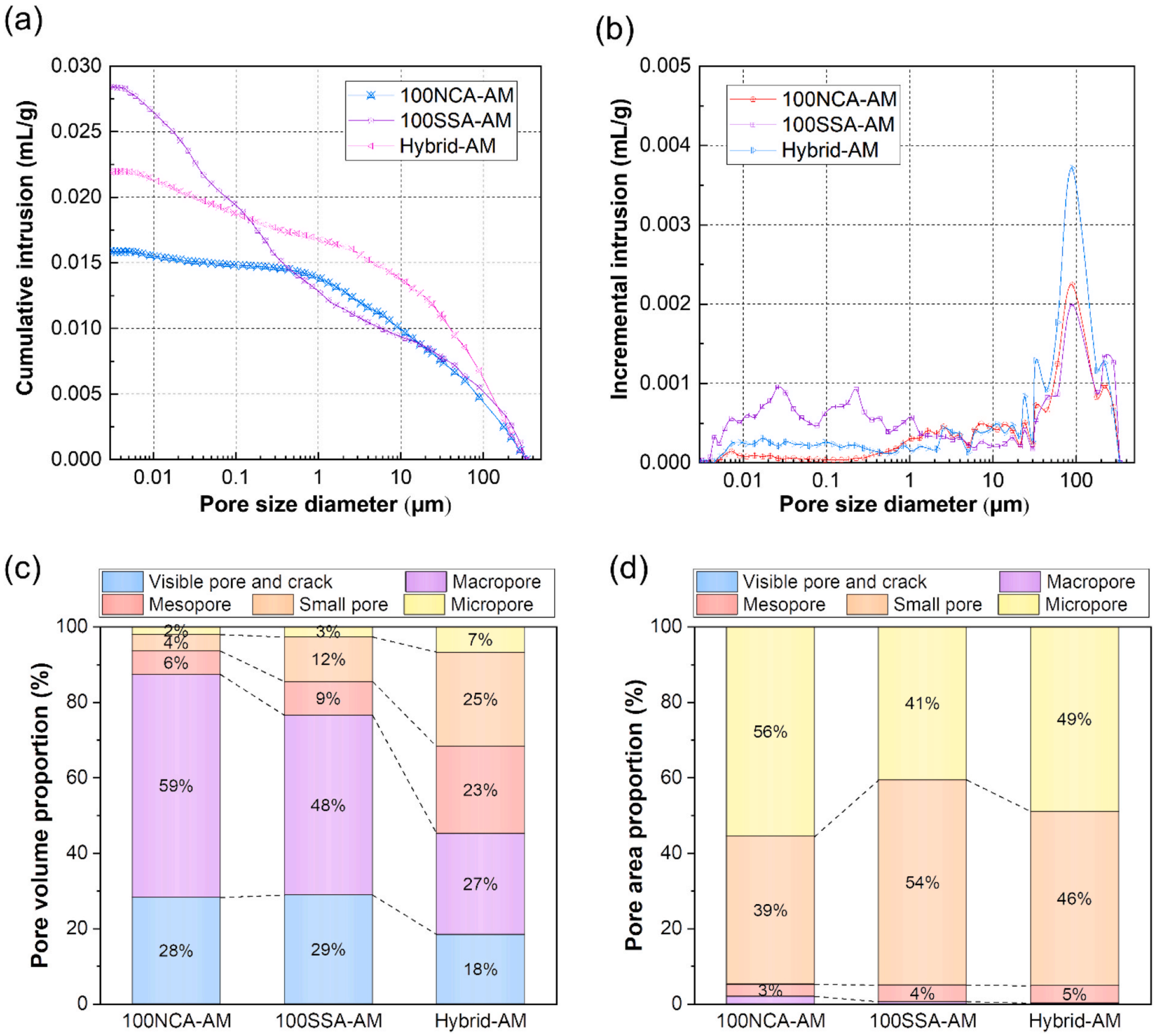

Fig. 10. The pore size and distribution characteristics of pore volume and pore area. (a) Cumulative pore volume (b) Pore size distribution (c) Pore volume proportion (d) Pore area proportion.

the pixels representing voids and solid phases. Fig. 11(a)-(c) illustrate the analysis of layer-by-layer porosity and the three-dimensional distribution of pores in the asphalt mixture, as revealed by CT slice scanning.

The results indicate that the overall porosity of 100SSA-AM is the highest, followed by Hybrid-AM, with 100NCA-AM being the lowest, consistent with the findings from the MIP test (see Section 3.2.1, Fig. 9). The pore distribution in all three asphalt mixtures follows a basin-like pattern along the specimen's height, with larger pores at both ends and smaller pores in the middle. The ends are approximately symmetrically distributed, aligning with the research findings of Fan et al. [51]. Specifically, the porosity at the ends of

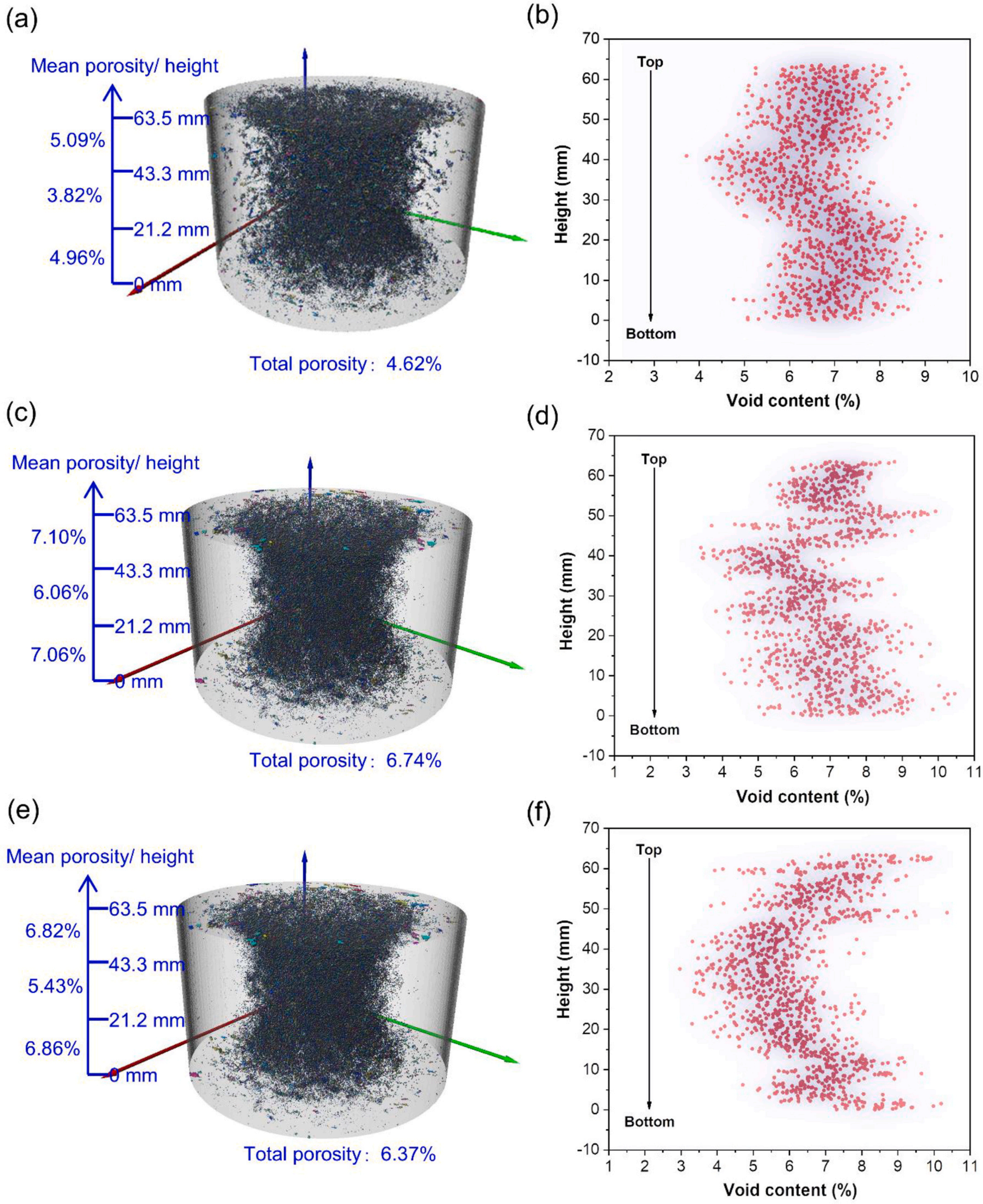

Fig. 11. Porosity distribution of specimen in the depth direction and three-dimensional diagram of pore; (a) and (b) 100NCA-AM; (c) and (d) 100SSA-AM; (e) and (f) Hybrid-AM.

the specimens is 16.6–33.2 % higher than in the middle. This may be attributed to the eccentric arrangement of the filler towards the ends during the compaction process, leading to a lower filler concentration and larger pores at the ends, while the middle is more compact with smaller pores. Additionally, uneven compaction may contribute to the increase in pore distribution from the middle to the ends.

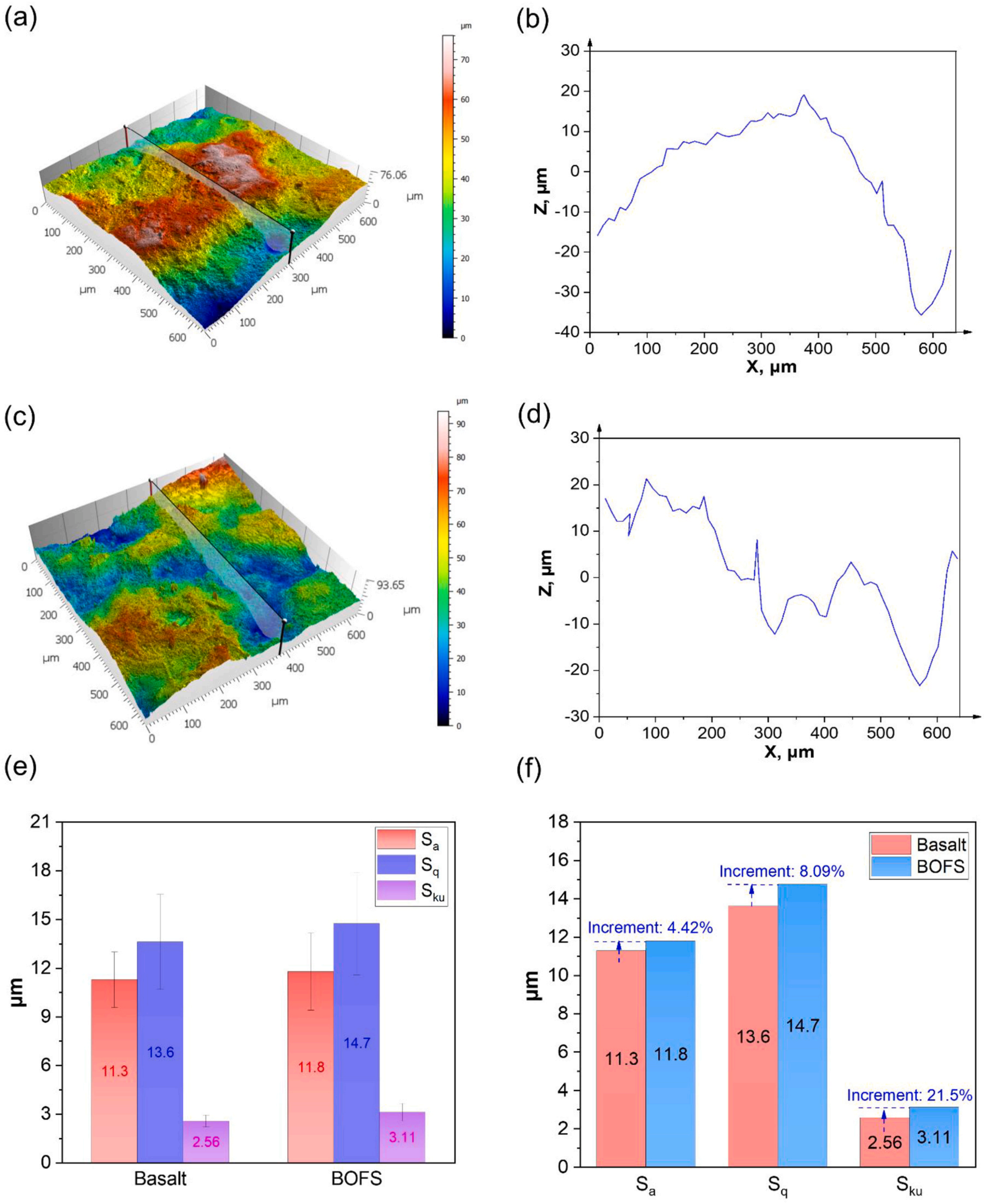

Fig. 12. Aggregate surface interface roughness analysis; (a) and (b) three-dimensional morphology and surface profiles of basalt; (c) and (d) three-dimensional morphology and surface profiles of BOFS; (e) and (f) Characterization parameters of aggregate surface morphology.

3.3. *Microstructure and element distribution of the ITZ*

3.3.1. *Interface roughness of aggregate surface*

Fig. 12(a)-(d) demonstrates that the basalt surface exhibits a dense and relatively smooth microstructure, characterized by a regular strip-like pattern of protrusions and depressions. In contrast, the BOFS surface displays granular protrusions and basin-shaped depressions that are randomly and sporadically distributed, with irregular height variations and more significant gaps between adjacent flake-like protrusions. Notably, the surface roughness parameters Sa and Sq for BOFS are 4.42 % and 8.09 % higher, respectively, than those for basalt, as shown in Fig. 12(e)-(f). This indicates that BOFS has a greater deviation from the baseline contour, resulting in a rougher surface profile. The kurtosis value (Sku) for BOFS exceeds three and is higher than that of basalt, suggesting a more complex microscale surface structure with sharper features at the edges of the depressions. These findings suggest that BOFS has a more intricate surface texture and morphology compared to basalt, potentially enhancing its adhesive properties in the ITZ, a phenomenon supported by Wu et al. [50].

3.3.2. *Interface micromorphology and fractal dimension of interface profile*

Fig. 13 illustrates the interfacial microstructure and the fractal dimension of the interface contour for three types of asphalt mixtures. The ITZ of 100NCA-AM displays a recessed area with a larger opening and significantly higher brightness. In contrast, the ITZ of 100SSA-AM and Hybrid-AM exhibits an uneven, undulating structure with relatively lower brightness values, as shown in Fig. 13 (a)-(c). These differences are related to the surface structure of the basalt and BOFS aggregates. Goldstein et al. [52] have indicated that in SEM images, brightness is associated with the electron emission characteristics of the sample surface; a more uniform surface reflects secondary emitted particles more effectively, resulting in higher brightness. Therefore, based on brightness, the ITZ of 100SSA-AM and Hybrid-AM is less uniform than that of 100NCA-AM. Fig. 13 (d) shows that the fractal dimension of the interface contour in Hybrid-AM is 7.03 % and 3.79 % higher than in 100NCA-AM and 100SSA-AM, respectively. This suggests that the ITZ in Hybrid-AM has a more

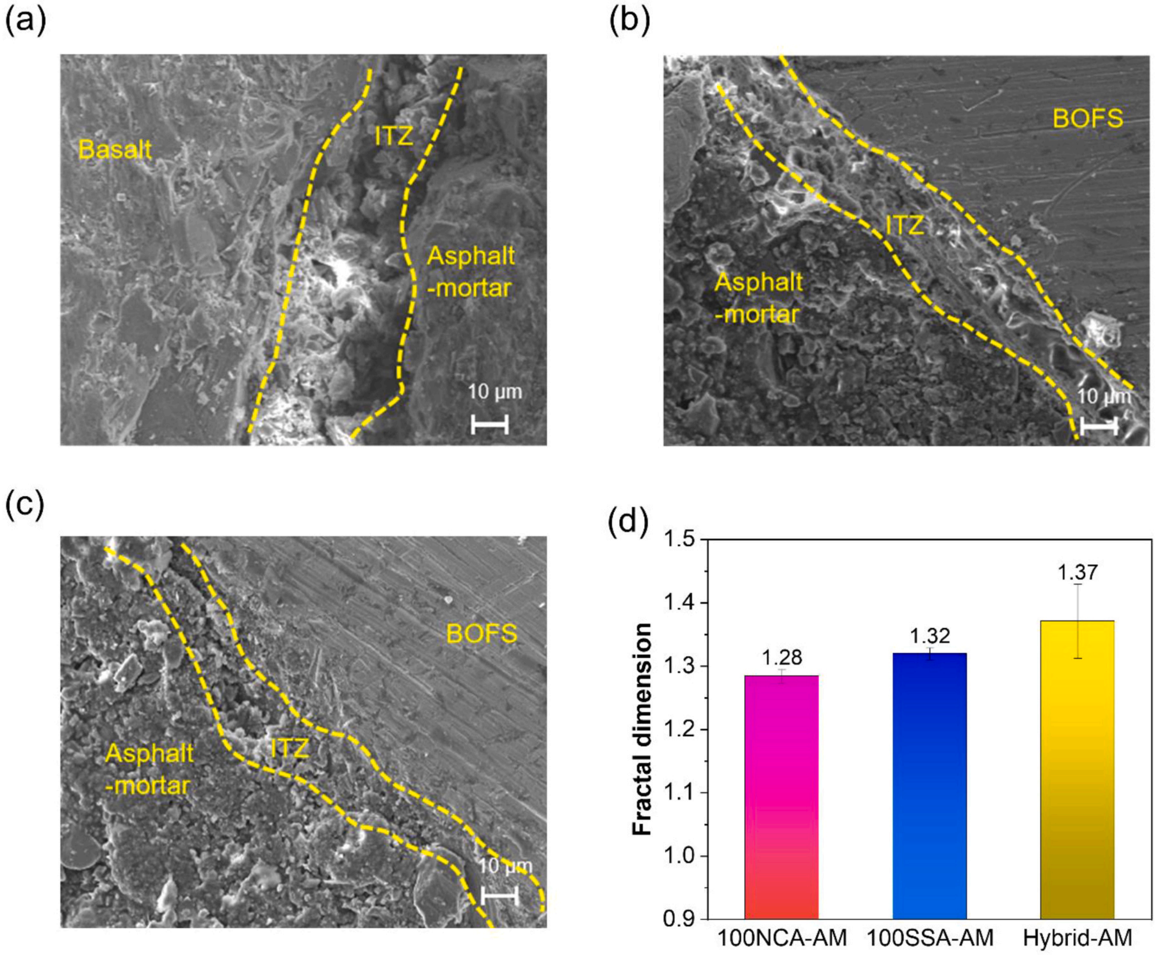

Fig. 13. The microstructure of ITZ and the fractal dimension of interfacial contour. (a) 100NCA-AM (b) 100SSA-AM (c) Hybrid-AM (d) The fractal dimension of interfacial contour.

complex and rough interface, potentially with more undulating microstructures. These features are beneficial for increasing the actual contact area between the asphalt mortar and aggregate, thereby enhancing interfacial friction and creating a superior aggregate interlocking effect.

3.3.3. Three-dimensional morphology analysis of ITZ

Fig. 14 presents the three-dimensional morphology and interface roughness of the ITZ in asphalt mixtures. The ITZ in 100NCA-AM is characterized by granular protrusions and narrow band depressions, with closely packed adjacent protrusions. In contrast, the ITZ in both 100SSA-AM and Hybrid-AM exhibits a similar pattern, featuring flake-like protrusions with larger spacing and continuous basin-like depressions. This similarity is likely due to the high proportion of BOFS in 100SSA-AM and Hybrid-AM, which leads to comparable wettability and adhesion of asphalt on the aggregate surface, resulting in a similar three-dimensional interfacial morphology. Additionally, compared to 100NCA-AM, the arithmetic mean height (Sa) of 100SSA-AM is reduced by 8.1 %, while the root mean square roughness (Sq) increases by 7.7 %. In Hybrid-AM, both the arithmetic mean height (Sa) and root mean square roughness (Sq) increase by 9.3 % and 27.4 %, respectively. Notably, the kurtosis and skewness values for 100SSA-AM and Hybrid-AM are significantly higher than those for 100NCA-AM, indicating greater interface non-uniformity in 100SSA-AM and Hybrid-AM. This difference can be attributed to the variations in roughness and chemical properties between BOFS and basalt aggregates, which affect the interfacial structure of the asphalt mixtures.

3.3.4. Chemical composition and element distribution of ITZ

Fig. 15 presents the SEM images and elemental distribution maps of the ITZ in asphalt mixtures. In these maps, higher brightness indicates a greater concentration of the respective element [22]. In Fig. 15 (a), the ITZ of 100NCA-AM near the aggregate shows a dense distribution of Si, Al, and O elements. In contrast, the ITZ of 100SSA-AM and Hybrid-AM near the aggregate displays higher concentrations of Ca and Fe, with only trace amounts of Si, as seen in Figs. 15(c) and 15(d). This difference is primarily due to the composition of basalt, a volcanic rock rich in silicates, while BOFS, a byproduct of steelmaking, is abundant in elements such as Ca and Fe. Additionally, the C element appears brighter in the ITZ near the asphalt-mortar region across all three types of asphalt mixtures, while it is dimmer near the aggregate. This is mainly because petroleum asphalt consists of hydrocarbons, including volatile organic compounds, polycyclic aromatic hydrocarbons, and n-alkanes [53], which are the primary reasons for the high content of C and H elements in asphalt mortar.

EDS line scanning tests on the asphalt mixtures reveal the elemental distribution signal intensities (including Fe, O, C, Si, Ca, and others) along the ITZ, as shown in Fig. 16. In Fig. 16(a), for 100NCA-AM, there is a significant decrease in the signal intensities of Si and O elements and a substantial increase in the C element signal intensity as one moves from the basalt to the asphalt mortar in the ITZ. This is primarily due to the significant difference in surface energy between silicates (basalt) and hydrocarbons (asphalt), which causes silicates to preferentially aggregate in the ITZ. Figs. 16(c) and 16(d) show that in 100SSA-AM and Hybrid-AM, the Fe element signal

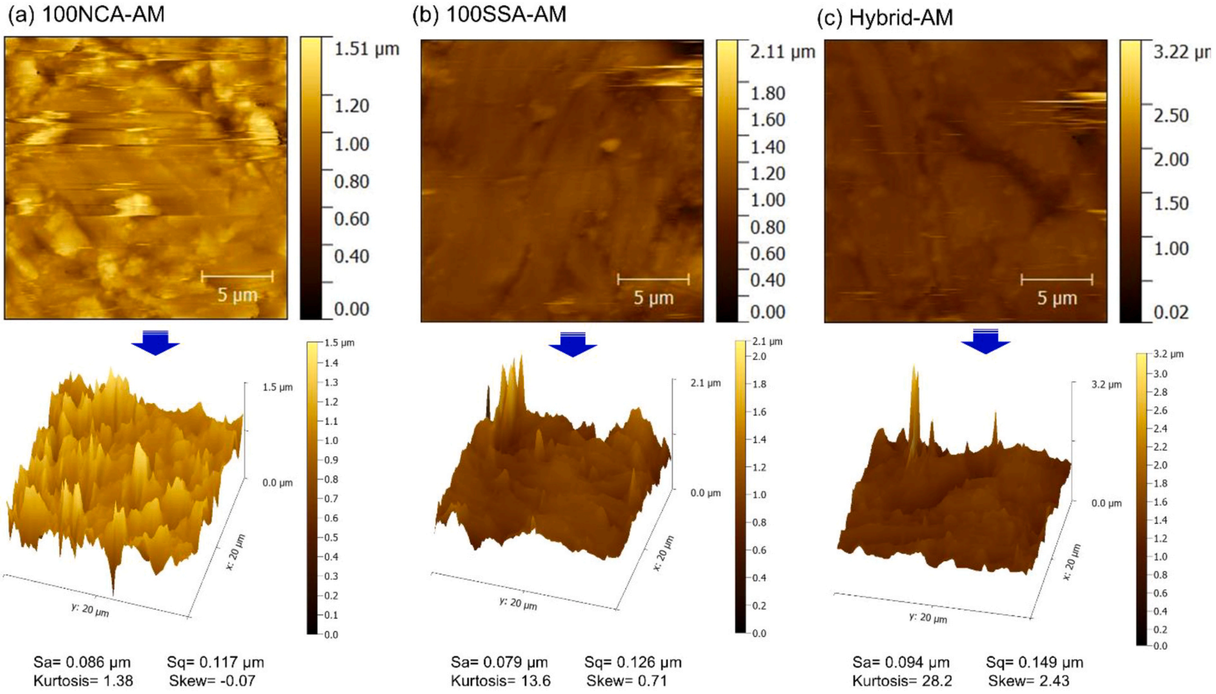

Fig. 14. Three-dimensional morphology and roughness of the ITZ between asphalt-mortar and aggregate; (a) 100NCA-AM; (b) 100SSA-AM; (c) Hybrid-AM.

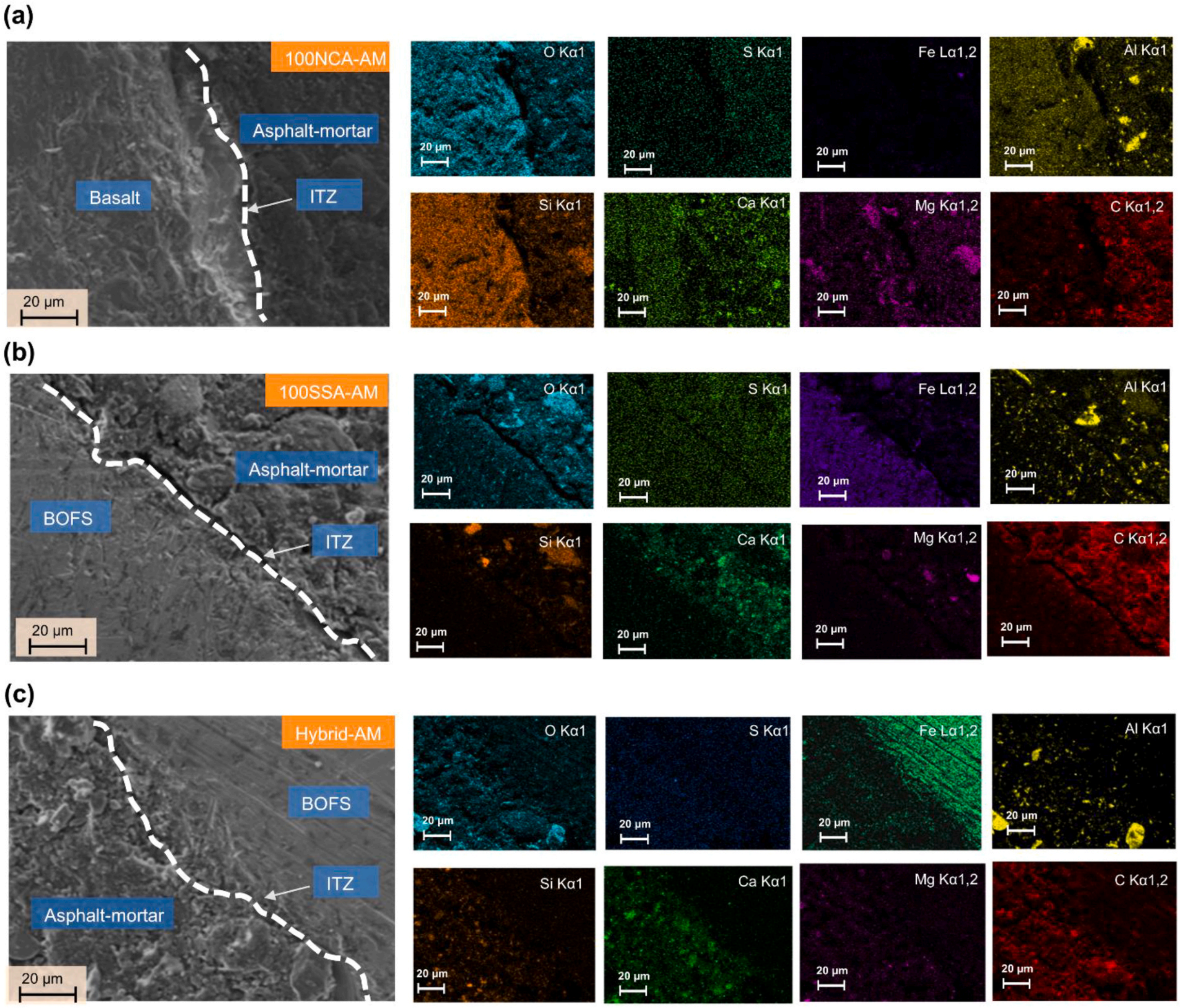

Fig. 15. EDS elemental of ITZ between aggregate and asphalt-mortar: (a) 100NCA-AM; (b) 100SSA-AM; (c) Hybrid-AM.

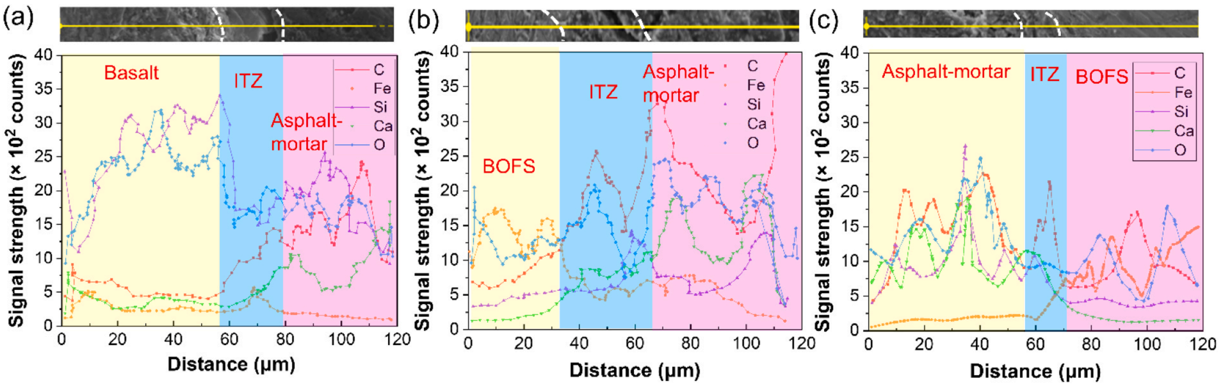

Fig. 16. EDS scanning results along the aggregate and asphalt-mortar line: (a) 100NCA-AM; (b) 100SSA-AM; (c) Hybrid-AM.

intensity in the ITZ decreases continuously from BOFS to the asphalt mortar, while the Si element signal intensity increases. This behavior is mainly attributed to the strong chemical affinity between the hydrocarbons in asphalt and the metal oxides in BOFS, leading to a strong adsorption effect and the migration of these elements within the ITZ. Additionally, compared to 100NCA-AM, the

ITZ width of 100SSA-AM increases by 10 μm, a 43.5 % increase, while the ITZ width of Hybrid-AM decreases by 6 μm, a 26.1 % decrease. The increase in ITZ width for 100SSA-AM is likely due to the irregular shape of BOFS, which creates more gaps during asphalt filling, affecting interface uniformity. Conversely, the fine basalt aggregate in Hybrid-AM may be more easily filled and encapsulated by asphalt, resulting in more contact points at the asphalt-aggregate interface, leading to a tighter interface connection and reduced ITZ width.

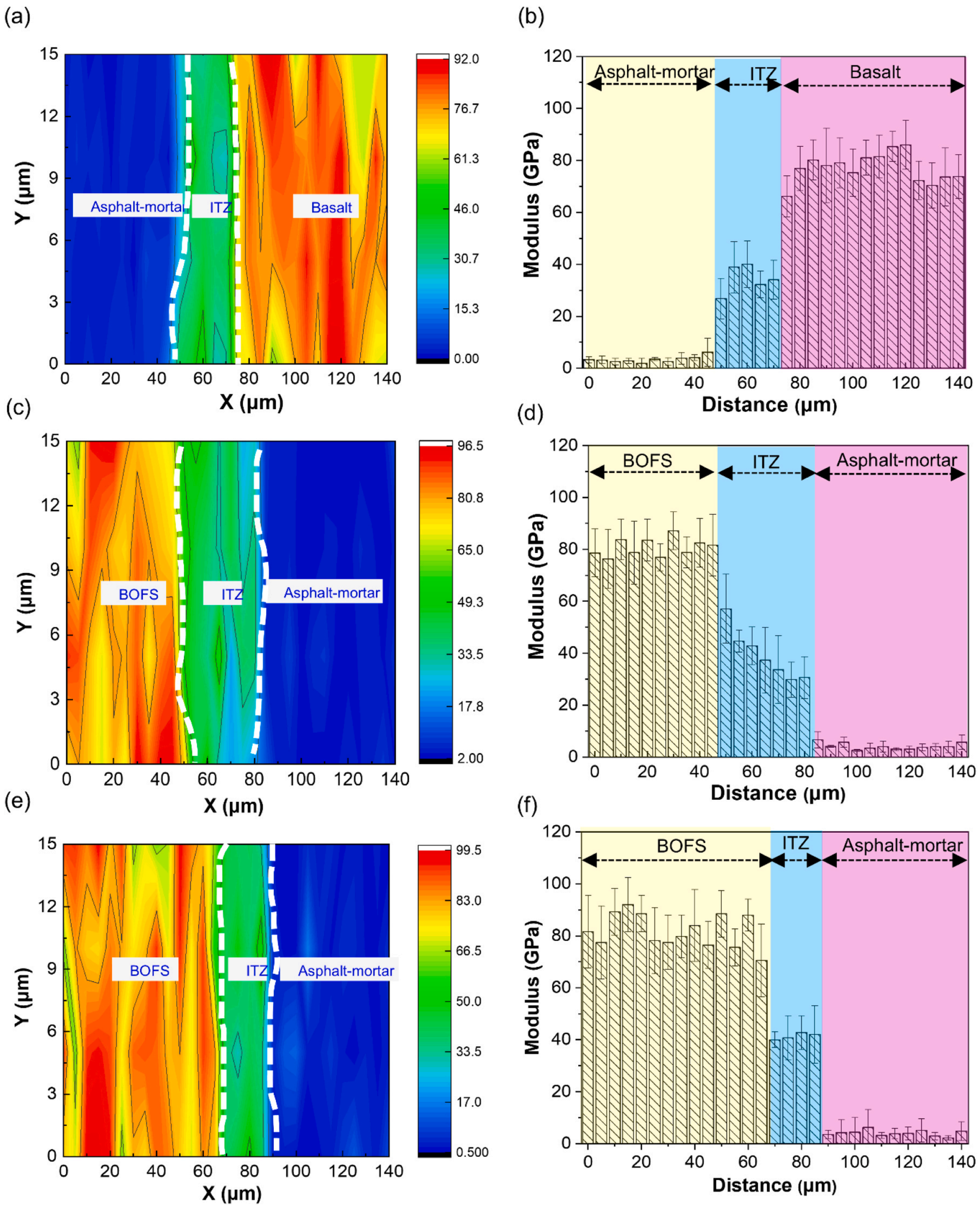

Fig. 17. Contour map and modulus distribution of ITZ grid nanoindentation between aggregate and asphalt mortar; (a) and (b)100NCA-AM; (c) and (d) 100SSA-AM; (e) and (f) Hybrid-AM.

3.4. Interfacial nanomechanics

Fig. 17 presents the ITZ width and indentation modulus of the asphalt mixtures. The results show that the ITZ width of 100SSA-AM increased by 10 μm, a 40 % increase, compared to 100NCA-AM, while the ITZ width of Hybrid-AM decreased by 5 μm, a 20 % reduction. These findings align with the conclusions from the EDS line scan (Section 3.3.4, see Fig. 16). The primary reason for this phenomenon is the higher surface roughness of BOFS, which leads to an uneven asphalt coverage on the aggregate surface, thereby increasing the ITZ width. Additionally, the combination of coarse BOFS and fine basalt in Hybrid-AM results in a rougher ITZ, which enhances electrostatic interaction forces at the molecular scale. Specifically, a rougher asphalt mixture interface strengthens van der Waals forces, improving interfacial adhesion in the ITZ and reducing its width [54]. Interestingly, the indentation modulus of the ITZ for 100SSA-AM and Hybrid-AM increased by 14.6 % and 20.3 %, respectively, compared to 100NCA-AM (see Figs. 17(b), 17(d), and 17(f)). This increase may be due to the formation of a denser microstructure in the ITZ of 100SSA-AM and Hybrid-AM at the microscopic level, enhancing the physical and mechanical interlocking between the asphalt mortar and aggregates.

3.5. Mechanism discussion

Table 3 summarizes the differences in interfacial performance between conventional asphalt mixtures and BOFS-asphalt mixtures at various scales. It is evident that, under the same gradation and asphalt-to-aggregate ratio, BOFS-asphalt mixtures exhibit a more favourable overall integrated performance despite having a higher void content, which is a disadvantage compared to conventional asphalt mixtures. Notably, Hybrid-AM demonstrates superior characteristics in macro and micro performance parameters such as indirect tensile strength, pore size distribution, and interfacial fractal dimension, outperforming the 100NCA-AM.

Generally, the ITZ between asphalt mortar and aggregates is the weakest part of asphalt mixtures and the primary area where cracks initiate and develop [22]. Appropriate aggregate morphology can help prevent cracking and rutting in asphalt pavements, enhancing their resistance to deformation and tensile strength [55,56]. A multi-scale perspective analysis of the failure mechanism of asphalt mixtures is shown in Fig. 18. The different physical properties of BOFS and basalt surfaces, such as the rough and complex texture of BOFS and the relatively smooth and dense surface of basalt, affect the interfacial compatibility of asphalt and aggregates. Specifically, the interconnected micropores in BOFS can selectively adsorb aromatic hydrocarbons and resins in the asphalt [57], which enhances the adhesion strength between asphalt and aggregates. Moreover, EDS line scanning and NI tests revealed that the ITZ width of 100SSA-AM is the largest, followed by 100NCA-AM, and the ITZ width of Hybrid-AM is the smallest. These differences in the asphalt-aggregate interfacial system caused by the aggregate characteristics of BOFS and basalt significantly affect the porosity, pore size distribution, and macroscopic failure mode of the asphalt mixture. In fact, there is a clear correlation between porosity, pore size distribution, and the shear behavior of the interface. As external load increases and shear stress is applied, the porosity of the asphalt mixture rises, and the expansion of internal micropores can develop into mesopores [58]. Hybrid-AM and 100SSA-AM contain more micropores and small to medium pores than 100NCA-AM (see Section 3.2.2, Fig. 10(c)), which enhances the internal microstructural stress skeleton, effectively strengthens the physical anchoring between asphalt and aggregate particles and improves the splitting strength of the asphalt mixture.

In practical engineering applications, due to the favourable asphalt-aggregate interfacial compatibility and dense micro-pore structure, Hybrid-AM exhibits superior comprehensive performance, making it particularly suitable for pavements with high crack and deformation resistance requirements. Applying 100SSA-AM is also a promising option for light traffic constructions, as it enhances the performance of the asphalt-aggregate interface and mechanical properties while utilizing industrial solid waste, such as steel slag. Additionally, temperature, loading rate, and type of asphalt can significantly affect the macroscopic mechanical properties of asphalt mixtures [59]. Therefore, the abovementioned factors in engineering design and application also should be considered to enhance the comprehensive performance of asphalt mixtures.

4. Conclusions

This study successfully applied fractal dimension theory to quantify the ITZ in BOFS-asphalt mixtures, revealing the underlying mechanisms of interfacial performance evolution through multi-scale analysis. These findings offer new insights into the macroscopic properties of BOFS-asphalt mixtures. The main conclusions are as follows:

1) In terms of macroscopic interfacial bonding performance, the splitting tensile strength of 100SSA-AM and Hybrid-AM increased by 22.2 % and 28.1 %, respectively, while the failure strain improved by 14.3 % and 5.9 %, and the crack resistance index increased by 13.5 % and 7.1 %, respectively. This suggests that the microstructure of BOFS can more effectively disperse stress under load, suppressing the initiation and propagation of cracks.
2) Concerning the microscale pore size structure, the total porosity of 100SSA-AM and Hybrid-AM increased by 58.4 % and 47.2 %, respectively, with a slight decrease in the fractal dimension of the pores and a significant increase in the volume ratio of micropores and small pores. This indicates that asphalt mixtures incorporating BOFS have higher porosity and lower tortuosity, which may impact their durability and resistance to fluid penetration.
3) Regarding interfacial micromorphology, the microsurface of BOFS-asphalt mixtures exhibits heterogeneous characteristics, whereas the basalt asphalt mixtures display a smooth, strip-like arrangement. Quantitative analysis of fractal dimensions reveals that compared to 100NCA-AM and 100SSA-AM, the fractal dimension of ITZ for Hybrid-AM is increased by 7.0 % and 3.8 %, respectively. This indicates that incorporating BOFS enhances the roughness and complexity of the ITZ.

Table 3
The differences in interfacial performance between conventional asphalt mixtures and BOFS-asphalt mixtures at various scales.

Performance characteristic	Parameters	Response*	100NCA-AM	100SSA-AM	Hybrid-AM
Macroscopic mechanical properties	Tensile strength	Relative increase, then slight increase	+	+ + +	+ + + +
	Failure strain	Relative increase, then slight decrease	+ +	+ + + +	+ + +
	Stiffness modulus	Slight increase, then significant increase	+	+ +	+ + + + +
	Cracking test index	Relative increase, then slight decrease	+ + +	+ + + + +	+ + + +
Microscopic pore structure	Porosity	Significant increase, then slight decrease	+	+ + + + +	+ + + +
	Pore fractal dimension	Slight decrease, then almost no effect	+ +	+	+
	Pore volume distribution	Relative decrease, then significant decrease	+ + + + +	+ + + +	+ +
Micromorphological characteristics	Interface fractal dimension	Relative increase, then slight increase	+	+ + +	+ + + +
	Interface roughness	Relative increase, then slight increase	+	+ + +	+ + + +
	Interface width	Significant increase, then significant increase	+ + +	+ + + + +	+
Interfacial nanomechanics	Interface indentation modulus	Significant increase, then relative increase	+	+ + + +	+ + + + +

[*] Note: All response descriptions are for the same gradation and asphalt-to-aggregate rati o conditions. '+ ' indicates the response level. The greater the number of '+ 's, the greater the response [2].

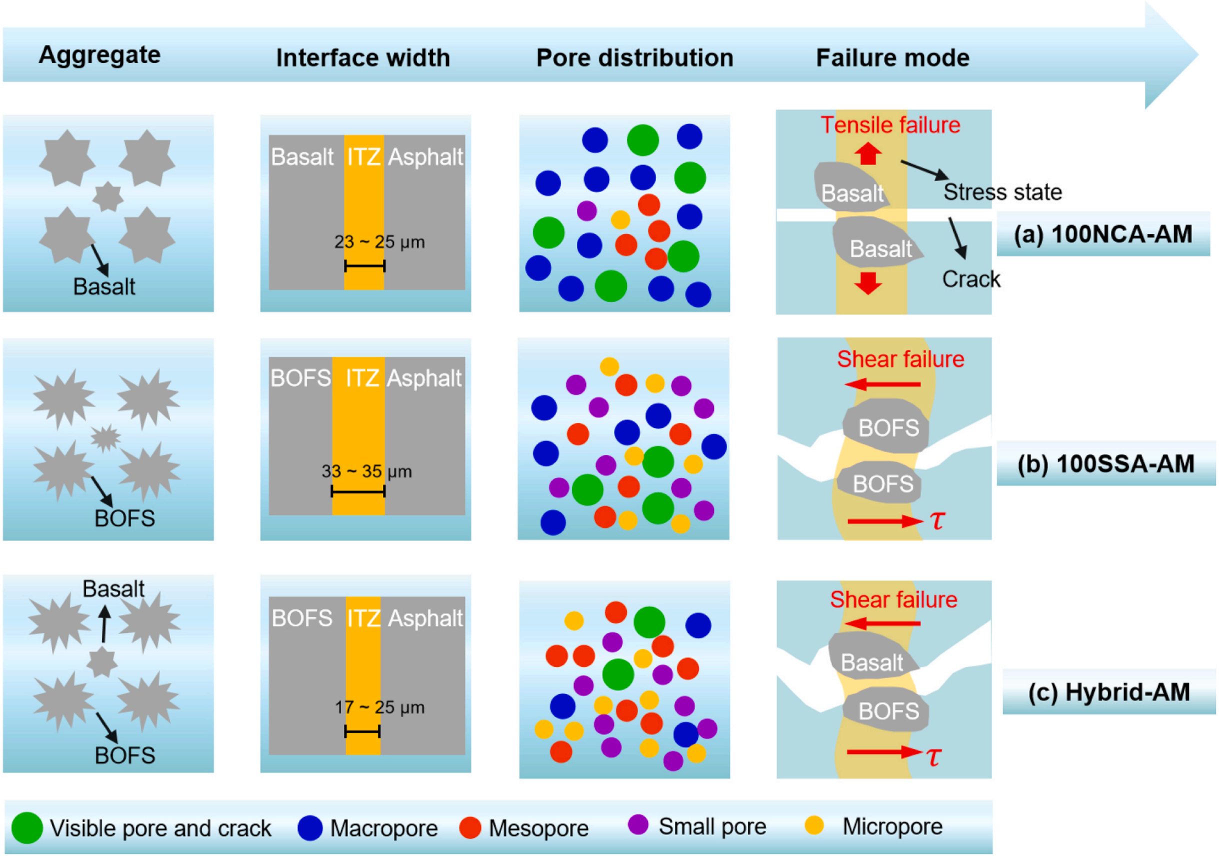

Fig. 18. Failure mechanism analysis of asphalt mixture from multi-scale perspective.

4) Considering interfacial elemental characteristics, the signal intensities of silicon and oxygen in the ITZ of 100NCA-AM are reduced while the signal intensity of carbon is increased. In contrast, the ITZ of 100SSA-AM and Hybrid-AM show a decrease in iron signal intensity and an increase in silicon signal intensity, reflecting changes in the chemical interactions at the material interface. At the nano-mechanical level, the ITZ indentation modulus of 100SSA-AM and Hybrid-AM is increased by 14.6 % and 20.3 % compared to 100NCA-AM, respectively. Additionally, the ITZ width of 100SSA-AM is increased by 43.5 %, while that of Hybrid-AM is decreased by 26.1 %. This suggests a more refined microstructure enhances the mechanical interlock between the asphalt mortar and the aggregate.

5) Future research can focus on the durability of BOFS asphalt mixtures under environmental conditions such as salt erosion, temperature fluctuations, and ultraviolet radiation, which is crucial for ascertaining their reliability in practical engineering applications. Additionally, advanced numerical simulation techniques like molecular dynamics simulation and finite element analysis can be employed to establish an interfacial mechanical model for BOFS asphalt mixtures. Analyzing interfacial failure behaviour under various loading conditions and predicting their performance in real-world applications represents another direction for future studies.

Abbreviations

Abbreviation	Name	Abbreviation	Name
ITZ	Interfacial Transition Zone	100SSM-AM	Full Proportion Steel Slag Asphalt Mixture
BOFS	Basic Oxygen Furnace Steel Slag	100NCA-AM	Full Proportion Basalt Asphalt Mixture
SEM	Scanning Electron Microscope	100Hybrid-AM	Asphalt Mixture of Coarse Aggregate Steel Slag and Fine Aggregate Basalt
AFM	Atomic Force Microscopy	OAC	Optimal Asphalt-to-aggregate Content
NI	Nanoindentation	IDT	Indirect Splitting Test
EDS	Energy Dispersive Spectroscopy	SBS	Styrene-Butadiene-Styrene
MIP	Mercury Intrusion Porosimetry	DTO	High-ductility, Ultra-thin Overlay
X-CT	X-ray Computed Tomography	TG	Thermogravimetry

CRediT authorship contribution statement

Yuan Meng: Writing – review & editing. **Jiawu Chen:** Writing – original draft, Software. **Ning Li:** Writing – review & editing. **Dong Lu:** Writing – review & editing, Supervision, Methodology. **Linjie Yu:** Writing – original draft, Formal analysis, Data curation. **Bin Lei:** Writing – original draft, Funding acquisition, Conceptualization. **Fulin Qu:** Writing – review & editing, Supervision, Project administration.

Declaration of Competing Interest

The authors declare that they have no known competing financial interests or personal relationships that could have appeared to influence the work reported in this paper.

Acknowledgements

The authors would like to acknowledge the supports from Innovative Research Group Project of the National Natural Science Foundation of China (52268043, 51968046) and the Chinese Scholarship Council (202306820047).

Data availability

Data will be made available on request.

References

[1] X. Xu, L. Kong, X. Li, B. Lei, B. Sun, X. Li, W. Dong, Analysis of carbon reduction effect of cement stabilized phosphogypsum base and cold recycled petroleum asphalt concrete pavement, Constr. Build. Mater. 433 (2024) 136696.

[2] F. Qu, W. Li, K. Wang, S. Zhang, D. Sheng, Performance deterioration of fly ash/slag-based geopolymer composites subjected to coupled cyclic preloading and sulfuric acid attack, J. Clean. Prod. 321 (2021) 128942.

[3] D. Lu, C. Fu, X. Jiang, Z. Chen, F. Qu, Y. Huo, Z. Leng, J. Zhong, Sustainable microwave-heating healing asphalt concrete incorporating functional aggregates and waste ferrite, Transp. Res. Part D: Transp. Environ. 129 (2024) 104117.

[4] B. Lei, L. Yu, Y. Guo, H. Xue, X. Wang, Y. Zhang, W. Dong, F. Dehn, W. Li, Triaxial mechanical behaviours and life cycle assessment of sustainable multi-recycled aggregate concrete, Sci. Total Environ. 923 (2024) 171381.

[5] Y. Meng, X. Zhu, Y. Zhang, Y. Su, F. Qu, C. Poon, J. Yan, D. Tsang, Valorizing inherent resources from waste streams for in-situ CO_2 capture and sequestration in the steel industry, J. Clean. Prod. 458 (2024) 142486.

[6] D. Lu, X. Jiang, F. Qu, Y. Huo, Mitigating sulfate ions migration in concrete: A targeted approach to address recycled concrete aggregate's impact, J. Clean. Prod. 442 (2024) 141135.

[7] M. Pasetto, A. Baliello, G. Giacomello, E. Pasquini, Sustainable solutions for road pavements: A multi-scale characterization of warm mix asphalts containing steel slags, J. Clean. Prod. 166 (2017) 835–843.

[8] K.A. Saha, M. Khan, K.P. Sarker, Value added utilization of by-product electric furnace ferronickel slag as construction materials: A review, Resour., Conserv. Recycl. 134 (2018) 10–24.

[9] Y. Huang, R. Bird, O. Heidrich, A review of the use of recycled solid waste materials in asphalt pavements, Resour., Conserv. Recycl. 52 (1) (2007) 58–73.

[10] C. Kambole, P. Paige, W.K. Kupolati, J.M. Ndambuki, A.O. Adeboje, Basic oxygen furnace slag for road pavements: A review of material characteristics and performance for effective utilisation in southern Africa, Constr. Build. Mater. 148 (2017) 618–631.

[11] E. Belhadj, C. Diliberto, A. Lecomte, Characterization and activation of basic oxygen furnace slag, Cem. Concr. Compos. 34 (2012) 34–40.

[12] J. Xie, S. Wu, J. Lin, Recycling of basic oxygen furnace slag in asphalt mixture: Material characterization & moisture damage investigation, Constr. Build. Mater. 36 (2012) 467–474.

[13] S. Amelian, M. Manian, S.M. Abtahi, A. Goli, Moisture sensitivity and mechanical performance assessment of warm mix asphalt containing by-product steel slag, J. Clean. Prod. 176 (2018) 329–337.
[14] D.F. Lin, L.H. Chou, Y.K. Wang, H.L. Luo, Performance evaluation of asphalt concrete test road partially paved with industrial waste - Basic oxygen furnace slag, Constr. Build. Mater. 78 (2015) 315–323.
[15] V. Haritonovs, M. Zaumanis, G. Brencis, J. Smirnovs, Performance of asphalt concrete with dolomite sand waste and BOF steel slag aggregate, Balt. J. Road. Bridge Eng. 8 (2) (2013) 91–97.
[16] M. Shahbazi, M. Rowshanzamir, S.M. Abtahi, S.M. Hejazi, Optimization of carpet waste fibers and steel slag particles to reinforce expansive soil using response surface methodology, Appl. Clay Sci. 142 (2017) 185–192.
[17] D. Jin, J. Wang, L. You, D. Ge, C. Liu, H. Liu, Z. You, Waste cathode-ray-tube glass powder modified asphalt materials: Preparation and characterization, J. Clean. Prod. 314 (2021) 127949.
[18] D. Jin, T.K. Meyer, S. Chen, K.A. Boateng, J.M. Pearce, Z. You, Evaluation of lab performance of stamp sand and acrylonitrile styrene acrylate waste composites without asphalt as road surface materials, Constr. Build. Mater. 338 (2022) 127569.
[19] D. Jin, K. Xin, L. Yin, S. Mohammadi, B. Cetin, Z. You, Performance of rubber modified asphalt mixture with tire-derived aggregate subgrade, Constr. Build. Mater. 449 (2024) 138261.
[20] D. Jin, L. Yin, S. Nedrich, K.A. Boateng, Z. You, Resurface of rubber modified asphalt mixture with stress absorbing membrane interlayer: From laboratory to field application, Constr. Build. Mater. 441 (2024) 137452.
[21] D. Jin, S. Mohammadi, K. Xin, L. Yin, Z. You, Laboratory performance and field demonstration of asphalt overlay with recycled rubber and tire fabric fiber, Constr. Build. Mater. 438 (2024) 136941.
[22] Q. Huang, Z. Qian, J. Hu, D. Zheng, L. Chen, M. Zhang, J. Yu, Investigation on the properties of aggregate-mastic interfacial transition zones (ITZs) in asphalt mixture containing recycled concrete aggregate, Constr. Build. Mater. 269 (2021) 121257.
[23] D. Lu, F. Qu, Y. Su, K. Cui, Nano-engineered the interfacial transition zone between recycled fine aggregates and paste with graphene oxide for sustainable cement composites, Cem. Concr. Compos. 154 (2024) 105762.
[24] Z. Chen, S. Wu, Y. Xiao, W. Zeng, M. Yi, J. Wan, Effect of hydration and silicone resin on Basic Oxygen Furnace slag and its asphalt mixture, J. Clean. Prod. 112 (2016) 392–400.
[25] M. Ameri, S. Hesami, H. Goli, Laboratory evaluation of warm mix asphalt mixtures containing electric arc furnace (EAF) steel slag, Constr. Build. Mater. 49 (2013) 611–617.
[26] X. Gong, Q. Liu, H. Wang, P. Wan, S. Chen, J. Wu, S. Wu, Synthesis of environmental-curable CO_2-based polyurethane and its enhancement on properties of asphalt binder, J. Clean. Prod. 384 (2023) 135576.
[27] D. Li, Y. Ding, J. Wang, Y. Shi, Z. Cao, G. Sun, B. Huang, Multiscale molecular simulations on the rejuvenation of recycled asphalt mixture: An insight into molecular impact of rejuvenators in aged asphalt binders, J. Clean. Prod. 414 (2023) 137621.
[28] J. Jiang, F. Ni, X. Gu, L. Yao, Q. Dong, Evaluation of aggregate packing based on thickness distribution of asphalt binder, mastic and mortar within asphalt mixtures using multiscale methods, Constr. Build. Mater. 222 (2019) 717–730.
[29] X. Wang, Y. Huang, L. Geng, M. Li, H. Han, K. Li, Q. Xu, Y. Ding, T. Zhang, Multiscale performance of composite modified cold patch asphalt mixture for pothole repair, Constr. Build. Mater. 371 (2023) 130729.
[30] X. Jiang, D. Lu, B. Yin, Z. Leng, Advancing carbon nanomaterials-engineered self-sensing cement composites for structural health monitoring: A state-of-the-art review, J. Build. Eng. (2024) 109129.
[31] JTG E20-2011, Standard test methods of bitumen and bituminous mixtures for highway engineering, Ministry of Transport of the People's Republic of China, 2011.
[32] JTG 3432-2024, Test methods of aggregates for highway engineering, Ministry of Transport of the People's Republic of China, 2024.
[33] Z. Chen, S. Wu, F. Li, J. Chen, Z. Qin, P. Ling, Recycling of Flue Gas Desulfurization residues in gneiss based hot mix asphalt: Materials characterization and performances evaluation, Constr. Build. Mater. 73 (2014) 137–144.
[34] W. Lou, B. Guan, Z. Wu, Dehydration behavior of FGD gypsum by simultaneous TG and DSC analysis, J. Therm. Anal. Calorim. 104 (2) (2011) 661–669.
[35] X. Wu, Z. Hong, X. Hou, L. Husen, Study on steel slag and fly ash composite Portland cement, Cem. Concr. Res. 29 (7) (1999) 1103–1106.
[36] V.J. Ferreira, A.S. Vilaplana, T. García, A. Aranda, C. Lausín, C., A.M. Lopez, G. Ferreira, Evaluation of the steel slag incorporation as coarse aggregate for road construction: technical requirements and environmental impact assessment, J. Clean. Prod. 130 (2016) 175–186.
[37] F. Zhou, S. Im, L. Sun, S. Tom, Development of an IDEAL cracking test for asphalt mix design and QC/QA, Road. Mater. Pavement Des. 18 (2017) 405–427.
[38] C. Panigrahy, A. Seal, K.N. Mahato, D. Bhattacharjee, Differential box counting methods for estimating fractal dimension of gray-scale images: A survey, Chaos, Solitons Fractals 126 (2019) 178–202.
[39] Y. Tian, X. Yan, D. Lu, T. Yang, Z. Wang, W. Li, Internal transport and corrosion behaviors of sulfate corrosion media carried by recycled aggregate in concrete, Constr. Build. Mater. 260 (2020) 120480.
[40] P. Zhan, X. Jing, J. Wang, C. Jiang, Multi-scale study on synergistic effect of cement replacement by metakaolin and typical supplementary cementitious materials on properties of ultra-high performance concrete, Constr. Build. Mater. 307 (2021) 125082.
[41] X. Wang, S. Jacobsen, J.Y. He, Z.L. Zhang, S.F. Lee, H.L. Lein, Application of nanoindentation testing to study of the interfacial transition zone in steel fiber reinforced mortar, Cem. Concr. Res. 39 (8) (2009) 701–715.
[42] W. Zhu, P. Bartos, Application of depth-sensing microindentation testing to study of interfacial transition zone in reinforced concrete, Cem. Concr. Res. 30 (8) (2000) 1299–1304.
[43] Y. Chao, J. Ren, X. He, S. Wu, Y. Su, J. Yang, Z. Jin, H. Qi, C. Tian, Z. Huang, Improved comprehensive adhesion performance of aggregate- recycled asphalt interface via incorporating steel slag, J. Mol. Liq. 404 (2024) 124958.
[44] D. Lu, X. Jiang, Z. Leng, Y. Huo, D. Wang, J. Zhong, Electrically conductive asphalt concrete for smart and sustainable pavement construction: A review, Constr. Build. Mater. 406 (2023) 133433.
[45] B. Ghanbarian, F. Liang, H. Liu, Modeling gas relative permeability in shales and tight porous rocks, Fuel 272 (2020) 117686.
[46] Y. Xue, S. Wu, H. Hou, J. Zha, Experimental investigation of basic oxygen furnace slag used as aggregate in asphalt mixture, J. Hazard. Mater. 138 (2) (2006) 261–268.
[47] P. Li, J. Ji, L. Wen, H. Chen, L. Bian, W. Zhou, Y. Wu, Quantitative characterization and evaluation of key physicochemical characteristics of steel slag, Constr. Build. Mater. 414 (2024) 134959.
[48] Z. Chen, S. Wu, Y. Xiao, M. Zhao, J. Xie, Feasibility study of BOF slag containing honeycomb particles in asphalt mixture, Constr. Build. Mater. 124 (2016) 550–557.
[49] N. Ma, Recycling of basic oxygen furnace steelmaking dust by in-process separation of zinc from the dust, J. Clean. Prod. 112 (2016) 4497–4504.
[50] S. Wu, Y. Xue, Q. Ye, Y. Chen, Utilization of steel slag as aggregates for stone mastic asphalt (SMA) mixtures, Build. Environ. 42 (7) (2007) 2580–2585.
[51] J. Fan, Y. Jiang, Y. Yong, T. Tian, K. Yuan, C. Deng, Investigation on triaxial numerical test method and dilatancy behavior of asphalt mixture, Constr. Build. Mater. 316 (2022) 125825.
[52] J. Goldstein, D.E. Newbury, J.R. Michael, N.W.M. Ritchie, J.H.J. Scott, D.C. Joy, Scanning Electron Microscopy and X-ray Microanalysis (M), Springer, 2017.
[53] R. Zhang, N. Tang, H. Zhu, Y. Xi, H. Cheng, J. Liu, R. Li, Compositional analysis and quantitative evaluation of organic emissions from asphalt materials: Improvements and refinements, J. Clean. Prod. 467 (2024) 142936.
[54] X. Zhou, G. Zhao, S. Tighe, M. Chen, S. Wu, S. Adhikari, Y. Gao, Quantitative comparison of surface and interface adhesive properties of fine aggregate asphalt mixtures composed of basalt, steel slag, and andesite, Constr. Build. Mater. 246 (2020) 118507.
[55] Y. Jiang, Y. Zhang, Y. Yi, T. Tian, J. Fan, J. Xue, Study of shear strength and gradation optimization of asphalt mixture based on uniaxial penetration numerical test, Constr. Build. Mater. 397 (2023) 132398.

[56] H. Yu, C. Zhang, G. Qian, J. Ge, X. Zhu, D. Yao, C. Shi, Characterization and evaluation of coarse aggregate wearing morphology on mechanical properties of asphalt mixture, Constr. Build. Mater. 388 (2023) 131299.

[57] C. Yang, J. Xie, S. Wu, S. Amirkhanian, X. Zhou, D. Kong, Q. Ye, J. Hu, Revelation and characterization of selective absorption behavior of bitumen to basic oxygen furnace slag, Constr. Build. Mater. 253 (2020) 119210.

[58] L. Wen, W. Cao, Y. Yang, Y. Li, Y. Liu, J. Huang, Experimental study on the shear behavior of the interface between asphalt concrete core wall and transition layer, Constr. Build. Mater. 440 (2024) 137469.

[59] F. Yin, J. Garita, A. Taylor, R. West, Refining the indirect tensile (IDT) N_{flex} Factor test to evaluate cracking resistance of asphalt mixtures for mix design and quality assurance, Constr. Build. Mater. 172 (2018) 396–405.